# UC Berkeley

## UC Berkeley Previously Published Works

**Title**

Multidimensional spectroscopy with attosecond extreme ultraviolet and shaped near-infrared pulses

**Permalink**

**Journal**

**ISSN**

**Authors**

Marroux, Hugo JB
Fidler, Ashley P
Neumark, Daniel M
et al.

**Publication Date**

**DOI**

Peer reviewed

# Multidimensional spectroscopy with attosecond extreme ultraviolet and shaped near-infrared pulses

Hugo J. B. Marroux[1,2], Ashley P. Fidler[1,2], Daniel M. Neumark[1,2]*, Stephen R. Leone[1,2,3]*

Dynamics following excitation with attosecond extreme ultraviolet (XUV) pulses arise from enormous numbers of accessible excited states, complicating the retrieval of state-specific time evolutions. We develop attosecond XUV multidimensional spectroscopy here to separate interfering pathways on a near-infrared (NIR) energy axis, retrieving single state dynamics in argon atoms in a two-dimensional (2D) XUV-NIR spectrum. In this experiment, we measure four-wave mixing signal arising from the interaction of XUV attosecond pulses centered around 15 eV with two few-cycle NIR pulses. The 2D spectrum is created by measuring the emitted XUV signal field spectrum while applying narrowband amplitude and phase modulations to one of the NIR pulses. Application of such a technique to systems of high dimensionality will provide for the observation of state-resolved pure electronic dynamics, in direct analogy to phenomena unraveled by multidimensional spectroscopies at optical frequencies.

## INTRODUCTION

Extreme ultraviolet (XUV) light pulses of few or sub-femtosecond duration are now routinely produced in both tabletop experiments and large facilities. With these pulses, one can investigate the dynamics of highly excited atomic and molecular states in which pure electronic dynamics, such as Auger decay (1, 2), autoionization (3, 4), and ionization (5), occur in only a few femtoseconds or less. High harmonic generation (HHG)–based experiments are capable of routinely producing isolated pulses that support durations <100 as (6) with sufficient timing stability and flux to efficiently probe these processes (7). The large bandwidth associated with these pulses creates complex coherent superpositions of states (wave packets) spanning multiple electronic and vibrational levels (8). Typical attosecond spectroscopy experiments use isolated attosecond pulses in combination with intense broadband near-infrared (NIR) pulses to preserve the time resolution provided by the attosecond pulse while compensating for its weak intensity. Attosecond transient absorption in which an XUV pulse is followed by a NIR pulse has been an especially powerful tool to study dynamics of excited states located in the XUV in both atomic and molecular systems (3, 8, 9). However, the temporal dependence observed in these experiments is complex because many couplings between excited states induced by the NIR pulses are spatially overlapped.

In an effort to separate the different types of interactions present in these experiments, four-wave mixing (4WM) using an attosecond XUV pulse and two NIR pulses has been reported previously to differentiate interaction schemes such as ladder, Vee, or lambda couplings between highly excited states of Ne, Ar, and $H_2$ (10–12). The different types of coupling satisfy phase-matching conditions and therefore can be spatially separated (13). Time evolution of the 4WM signal spectrum shows strong quantum beat oscillations due to emission pathway interferences, indicating that each emission frequency reports on the time evolution of several components of the initial wave packet created by the broadband pulses.

To identify each state and retrieve the individual time evolutions of states comprising the wave packet, new techniques that resolve transition energies while maintaining optimal time resolution are required. At lower excitation energies, the development of multidimensional optical and infrared spectroscopy enables one to unravel eigenstates and their couplings, ultrafast energy transfer, and chemical exchange dynamics (14–16). The most prevalent version of these experiments combines three broadband pulses interacting with a sample to create a macroscopic nonlinear polarization, which emits an electromagnetic field (signal field). Two-dimensional (2D) spectra are retrieved by scanning the various time delays to record free induction decay (FID) oscillations. A direct transposition of this coherent method (where phase-sensitive detection is used) into the XUV using multiple attosecond pulses is currently out of reach because of the high frequency of the FID and the associated timing stability required, although fully collinear arrangements show promise (17). Experiments capable of creating intense enough attosecond pulses to drive the nonlinear process also still need development.

Here, we translate the methodology of multidimensional spectroscopy to the XUV regime mixed with NIR pulses. We carry out 4WM experiments on Ar using attosecond XUV pulses spanning 14 to 16 eV and two intense femtosecond NIR pulses, one of which is pulse-shaped, to create 2D spectra that allow for the identification of individual eigenstates contributing to bright- and dark-state wave packets. The 2D NIR-XUV spectrum is formed by recording the emitted 4WM XU pectrum as a function of the NIR modulation energy. Using narrowband spectral phase and amplitude modulation of one of the NIR beams, emission pathways contributing to the nonlinear 4WM signal are separated on the NIR energy axis. Features of this 2D spectrum report on the time evolution of a single state composing the initial wave packet created by the broadband XUV attosecond pulses. This frequency domain method does not involve phase-sensitive detection and therefore circumvents technical challenges associated with phase stability in the XUV. The suppression of quantum beats in the time evolution of the 2D spectral features and the retrieval of invariant time evolution verify that the multidimensional experiment can decompose the initial wave packet into its individual components. Energy resolution as small as 1.4 to 2.2 meV in the NIR (depending on the central frequency) and 20 meV in the XUV is attained, while the sub–6-fs time resolution of the experiment is preserved.

[1]Department of Chemistry, University of California, Berkeley, Berkeley, CA 94720, USA. [2]Chemical Sciences Division, Lawrence Berkeley National Laboratory, Berkeley, CA 94720, USA. [3]Department of Physics, University of California, Berkeley, Berkeley, CA 94720, USA.
*Corresponding author. Email: srl@berkeley.edu (D.M.N.); dneumark@berkeley.edu (S.R.L.)
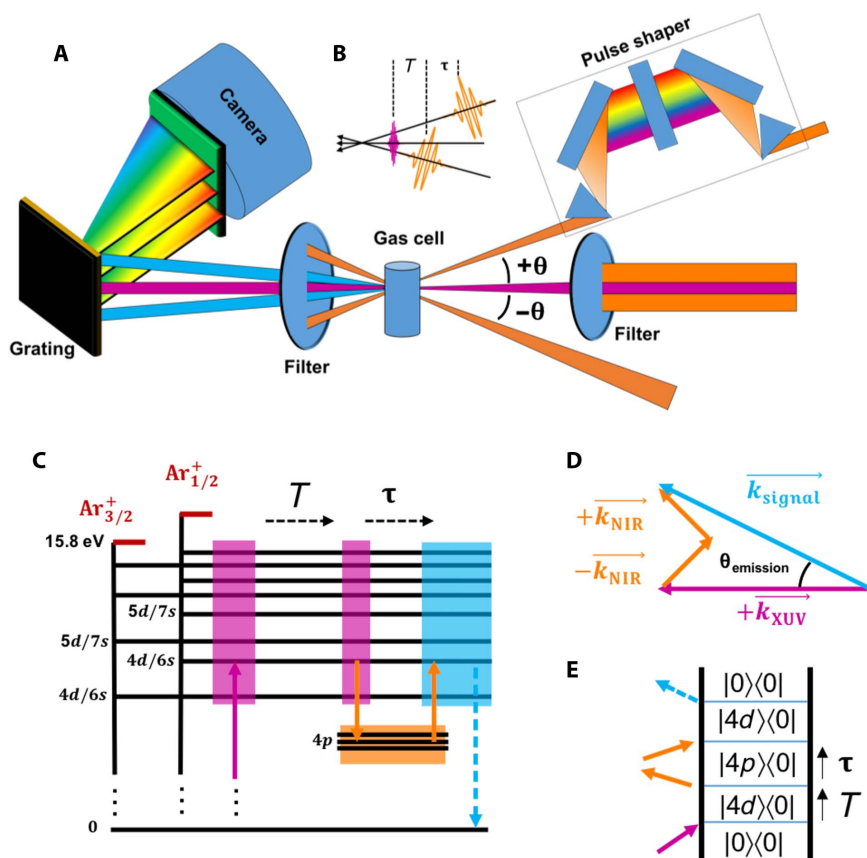
**Fig. 1. Experiment description.** (**A**) Experiment design. In the non-multidimensional experiment, the pulse shaper is bypassed. (**B**) Geometry and timing diagram used over the course of the study. (**C**) Energy diagram. The shaded areas represent the wave packet created by the corresponding broadband pulse. (**D**) Phase-matching geometry. (**E**) Example of a double-sided Feynman diagram leading to 4WM signal emission.

## RESULTS

Figure 1A shows a schematic of the experiment. A pulse train of ≤3 XUV attosecond pulses covering 14 to 16 eV (purple) generated by HHG from a 6-fs NIR field is directed into an argon-filled gas cell. Residual collinear NIR light from the HHG cell is blocked by a removable indium filter. Two NIR pulses are also incident on the argon-filled gas cell, and each forms an angle of ±17.5 mrad with the XUV beam. After the cell, the NIR fields are blocked by a second indium filter, while the incident (purple) and emitted (blue) XUV fields are dispersed on a cylindrical grating and detected by an x-ray charge-coupled device (CCD) camera. In the multidimensional experiments, a pulse shaper based on a spatial light modulator (SLM) is included in one of the incident NIR arms. In the several experiments presented here, only one of the time delays $T$ or $\tau$ in Fig. 1B is varied.

In a preliminary experiment where no pulse shaper is used, the two NIR pulses are coincident ($\tau = 0$), and $T$, the delay between the XUV and two NIR pulses, is varied. At $t = 0$, the broadband XUV pulse creates a wave packet comprising argon bright $ns$/$nd$ Rydberg state series, as indicated by the purple shaded area in the energy level diagram in Fig. 1C. At $t = T$, the two NIR pulses (orange arrows in Fig. 1C) couple the bright-state wave packet to the $4p$ dark-state manifold and back to the $ns$/$nd$ bright-state manifold. The nonlinear polarization resulting from one XUV interaction and two NIR interactions emits XUV radiation, that is, the 4WM signal field (blue) (*10*). In this experimental geometry, the phase matching condition shown in Fig. 1D spatially

separates the 4WM signals from the incident XUV field (*11*). All the incident pulses propagate in the same plane such that, for example, 4WM radiation is emitted in this plane with an angle of $\theta_{emission} = \frac{2k_{IR}\theta}{k_{XUV}}$ from the incident XUV field (in the small-angle limit). The emitted and incident fields are diffracted by the grating and imaged onto an X-ray CCD camera to simultaneously record all the spectra. The different response orders are displaced vertically on the camera chip, while the XUV wavelength is recorded on the horizontal axis. A double-sided Feynman diagram in Fig. 1E describes one of the interaction pathways yielding the emission of a signal field. Because of the broad bandwidth of the three pulses, many pathways involving different bright and dark states contribute to the 4WM signal.

Camera images at $T = 0$ are shown in Fig. 2A at NIR peak power intensities of $3 \times 10^{12}$ W/cm$^2$. The discrete features above and below the central XUV pulse spectrum in Fig. 2A correspond to square law (homodyned) detection of the 4WM signal. The time evolution of the 4WM signal when $\tau = 0$ and $T$ is varied is shown in Fig. 2B. We observe quantum beats corresponding to coherent wave packet dynamics created by the XUV pulse, similar to those observed in previous work (*11*).

To transform this setup into a multidimensional experiment, we introduce a pulse shaper to independently manipulate the spectral amplitude and phase of one of the two NIR pulses, as shown in Fig. 1A. One XUV emission spectrum (4WM) is collected with an unmodulated NIR spectrum $S(1, 0, \omega_{NIR}, \omega_{XUV})$, where the first two variables are the spectral amplitude and phase applied by the pulse shaper
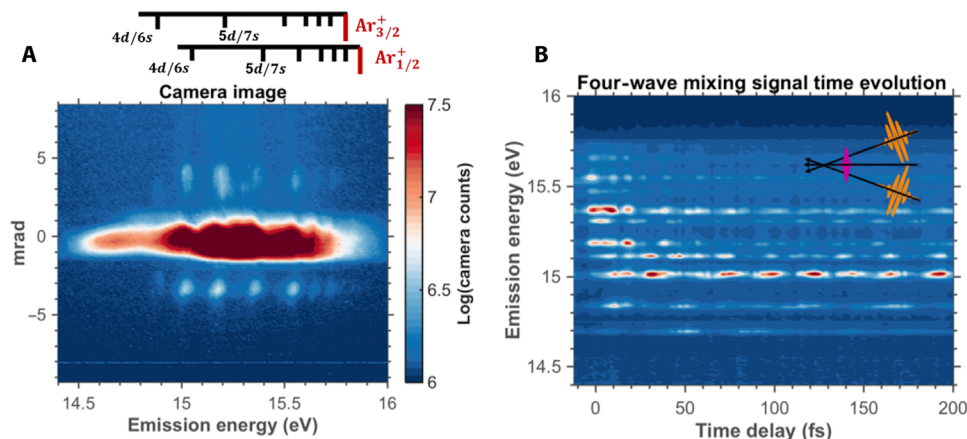
**Fig. 2. Spatial separation of interaction orders and 4WM time evolution.** (**A**) Camera images at time 0 for $3 \times 10^{12}$ W/cm$^2$. (**B**) Time evolution of the 4WM signal. In this experiment, $\tau$ is set to 0 and $T$ is scanned as indicated by the inset.

within a narrow band centered around $\omega_{NIR}$ and $\omega_{XUV}$ is the frequency of the XUV 4WM emission. A second XUV emission spectrum is collected with a narrow part of the NIR spectral amplitude set to zero [$S(0, 0, \omega_{NIR}, \omega_{XUV})$]. A third XUV emission spectrum is collected with a narrow part of the NIR spectral phase set to $\pi$ [$S(1, \pi, \omega_{NIR}, \omega_{XUV})$]. We obtain a cumulative analyzed signal as described by Eq. 1, the full derivation of which is shown in the Supplementary Materials

$$\begin{aligned} \text{Signal}(\omega_{NIR}, \omega_{XUV}) &= S(1, 0, \omega_{NIR}, \omega_{XUV}) + S(1, \pi, \omega_{NIR}, \omega_{XUV}) \\ &- 2*S(0, 0, \omega_{NIR}, \omega_{XUV}) \end{aligned} \quad (1)$$

Each XUV spectrum in Eq. 1 is collected over 1000 laser pulses for each modulation frequency at particular time delays. To minimize signal fluctuations, we consecutively collect multiple XUV spectra with phase modulations [$S(1, 0, \omega_{NIR}, \omega_{XUV})$] and [$S(1, \pi, \omega_{NIR}, \omega_{XUV})$] before acquiring the spectrum with amplitude modulation [$S(0, 0, \omega_{NIR}, \omega_{XUV})$]. We repeat this so that, at a single modulation frequency ($\omega_{NIR}$), 20,000 laser pulses are coadded to attain a desirable signal-to-noise ratio of at least 5 across the spectrum. By scanning $\omega_{NIR}$ and computing Eq. 1 for each frequency, we obtain a 2D map correlating NIR interaction energy and XUV emission energy at a specific time delay. The 6-fs duration of the shaped NIR pulse is preserved by compressing the pulse with the shaper itself (cf. the Supplementary Materials for pulse characterization) (18).

We use two different configurations here, configuration I, which probes dark states accessed by one XUV photon and one NIR photon, and configuration II, which probes bright states accessed directly by one XUV photon. Configuration I involves a slight modification of the optical layout in Fig. 1A. By removing the metal filter after the HHG cell, the copropagating NIR beam collinear with the XUV pulse serves as one of the NIR interactions that give rise to a 4WM signal. The other NIR interaction comes from the noncollinear beam in Fig. 1A that passes through the pulse shaper, while the second noncollinear beam is blocked. In this geometry, the collinear NIR pulse is automatically synchronized with the XUV pulse ($T = 0$) and creates a wave packet in the $4p$ dark states by two photon transitions; the second shaped NIR pulse projects this wave packet onto the bright states at a variable time delay $\tau$, emitting 4WM radiation at an angle $\theta_{emission} = \frac{k_{IR}\theta}{k_{XUV}}$. An emission spectrum for this experiment is shown in Fig. 3A, with

the pulse sequence and the experimental geometry in the corresponding inset. At a fixed time delay of $\tau = 200$ fs, we obtain the 2D map in Fig. 3B using the pulse shaping method described above. With the convention chosen, negative signal corresponds to a decrease of emission. Because of destructive interferences between emission pathways, features in the emission spectrum in Fig. 3A can have a low intensity and are therefore difficult to identify at a single time delay, but they appear in the 2D spectrum. For example, the feature at 14.7 eV is difficult to discern from the baseline in Fig. 3A, while it appears as a clear feature in the 2D spectrum in Fig. 3B.

The geometry for configuration II is the same as that in Fig. 1 (three noncollinear beams). The three pulses are each separated by 60 fs (that is, $T = \tau = 60$ fs) such that the XUV arrives first, the shaped NIR pulse arrives second, and the unshaped NIR pulse arrives last. The choice of the 60-fs time delay ($\tau$) aims to reduce the experiment susceptibility to time delay drift during data collection. The emission spectrum and the corresponding 2D spectrum for this experiment are shown in Fig. 3 (C and D, respectively). Here again, the negative features correspond to a decrease of emission. In both bright- and dark-state spectra in Fig. 3 (B and D), all the features are negative. Note that in Fig. 3B, the negative features lie on diagonal lines of unity slope, whereas in Fig. 3D, these features lie on horizontal lines at discrete NIR energies. The origin of these trends is explained below.

In Fig. 4, we compare the time evolution (with $\tau$ varied and $T = 0$) of the dark-state feature at (14.85 eV; 1.76 eV) of the 2D spectrum in Fig. 3B to that of the total emission at 14.85 eV. In Fig. 4A, using the synthesized signal with the shaped pulse in Eq. 1, the oscillations are suppressed, indicating that in the 2D measurement, a single component of the initial wave packet is isolated, as discussed in the following section.

Finally, in Fig. 5, we compare time traces (where $\tau$ is varied and $T = 0$) of the dark-state emission features at 15.02 and 15.38 eV in Fig. 3A when the NIR pulse spectrum is phase-modulated at one frequency, 2.04 eV. From the 2D spectrum in Fig. 3B, the emission at 15.02 eV is not affected by the modulation at 2.04 eV, while the feature at 15.38 eV is.

## DISCUSSION

The spectra in Fig. 3 (A and B) are collected in configuration I with collinear and time-coincident XUV and unshaped NIR pulses ($T = 0$). The shaped noncollinear NIR pulse probes the dark-state wave packet
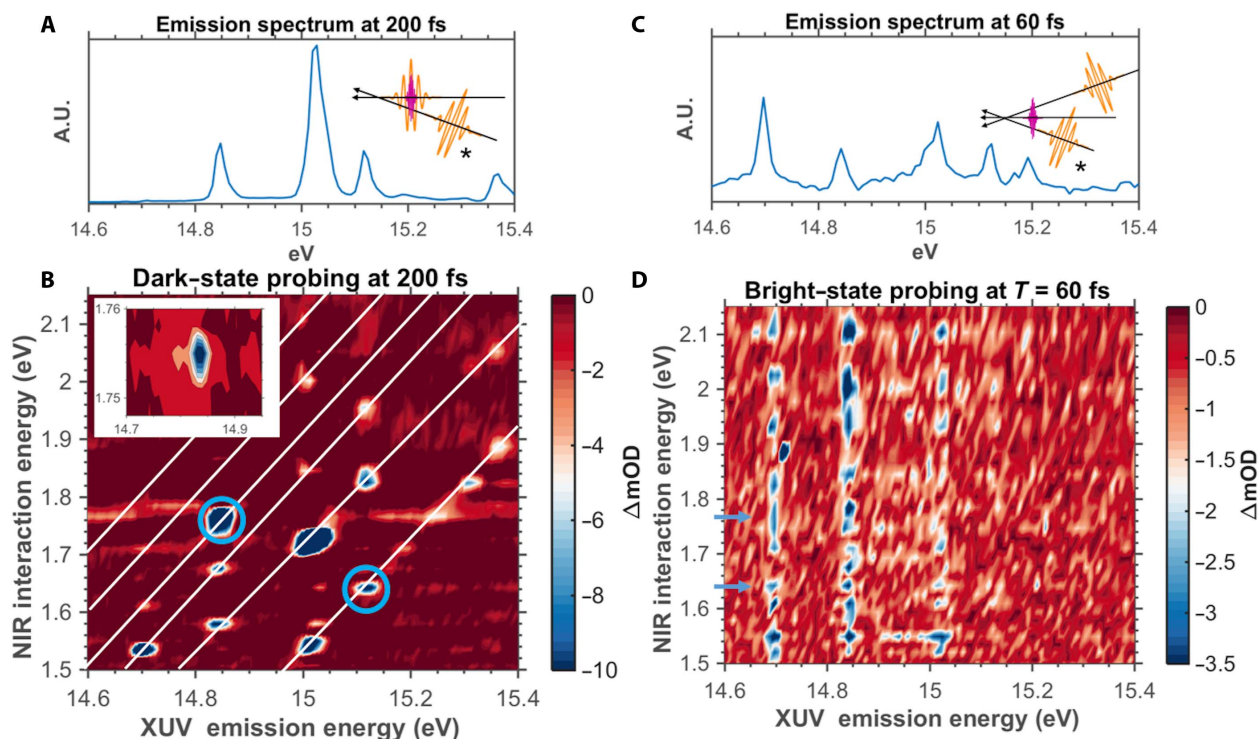
**Fig. 3. Bright- and dark-state 2D spectra.** (**A**) 4WM emission spectrum of the dark-state wave packet obtained with an unshaped pulse. The geometry and timing of the experiment in configuration I ($T = 0$, $\tau = 200$ fs) are shown in the inset. The shaped pulse in the 2D experiment is indicated by an asterisk. A.U., arbitrary units. (**B**) 2D spectrum obtained from (A) in milli optical density (mOD). White lines link features originating from the same dark state. The main spectrum was collected with an SLM pixel binning of 10 pixels, while the inset spectrum was collected without pixel binning and shows the feature at (14.85 eV; 1.755 eV). The blue circles indicate the features following the time evolutions of $[^2P_{1/2}]4p$ and $[^2P_{3/2}]4p$. (**C**) Bright-state emission spectrum obtained with an unshaped pulse and using the geometry and timing of configuration II ($T = 60$, $\tau = 60$ fs) depicted in the inset. (**D**) 2D spectrum probing the bright-state wave packet at $T = 60$ fs obtained by shaping the pulse indicated by an asterisk in the inset of (C). The blue arrows indicate features following the time evolution of $[^2P_{3/2}]5d/7s$ and $[^2P_{3/2}]4d$.
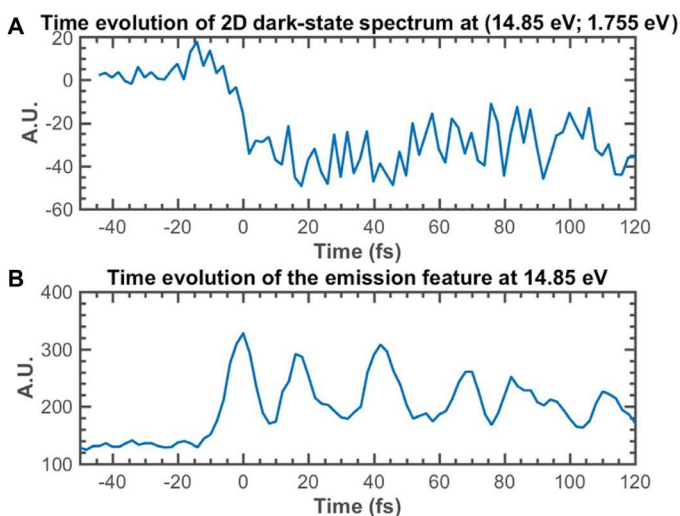


**Fig. 4. Separation of emission pathways and suppression of quantum beats.** (**A**) Time evolution of the dark-state 2D spectral feature at (14.85 eV; 1.76 eV). (**B**) Time evolution of the emission feature at 14.85 eV in the non-multidimensional experiment. The coherent sum of emission pathways leads to quantum beat oscillation in the time evolution of the emission line in (B). Quantum beat oscillations are not present in the time evolution of the 2D spectral feature in (A), indicating an efficient pathway separation.

after a time delay $\tau$. The 2D spectrum in Fig. 3B shows strong negative optical density features at NIR resonant frequencies corresponding to a decrease of XUV emission. The total XUV emission arises from interactions involving the entire dark-state wave packet (orange shaded area in Fig. 1C). When pulse shaping is applied at a NIR energy corresponding to a specific dark state to bright state transition (that is, orange up arrow in Fig. 1C), XUV emission from the bright state is depleted. The probed dark-state energy can be calculated from the 2D spectral features by taking the difference between the energies of the XUV emission and NIR interaction. Hence, the depleted features lie on diagonal lines of unity slope, as shown in Fig. 3B. Six different dark states are accessible in the experiment: four with $(^2P_{3/2})$ $4p$ character at 12.91, 13.00, 13.09, and 13.15 eV and two with $(^2P_{1/2})$ $4p$ character at 13.27 and 13.48 eV. Note that each of these values corresponds to the $x$ intercept of one of the diagonal lines.

The ability to discern individual dark states depends on the frequency resolution on the NIR axis, which is defined by the pulse shaper accuracy. The SLM is composed of 640 pixels capable of modulating spectral phase and amplitude. Spectra in Fig. 3 (B and D) are collected by binning 10 pixels together to decrease the acquisition time. A scan of the features at 14.85 and 1.76 eV collected without binning is provided in the inset of Fig. 3B. For this high-resolution scan, the frequency resolution in the NIR dimension is as small as 1.4 and 2.2 meV, which is still larger than the natural linewidth of the Rydberg states considered because of their microsecond lifetimes (*19*). The resolution
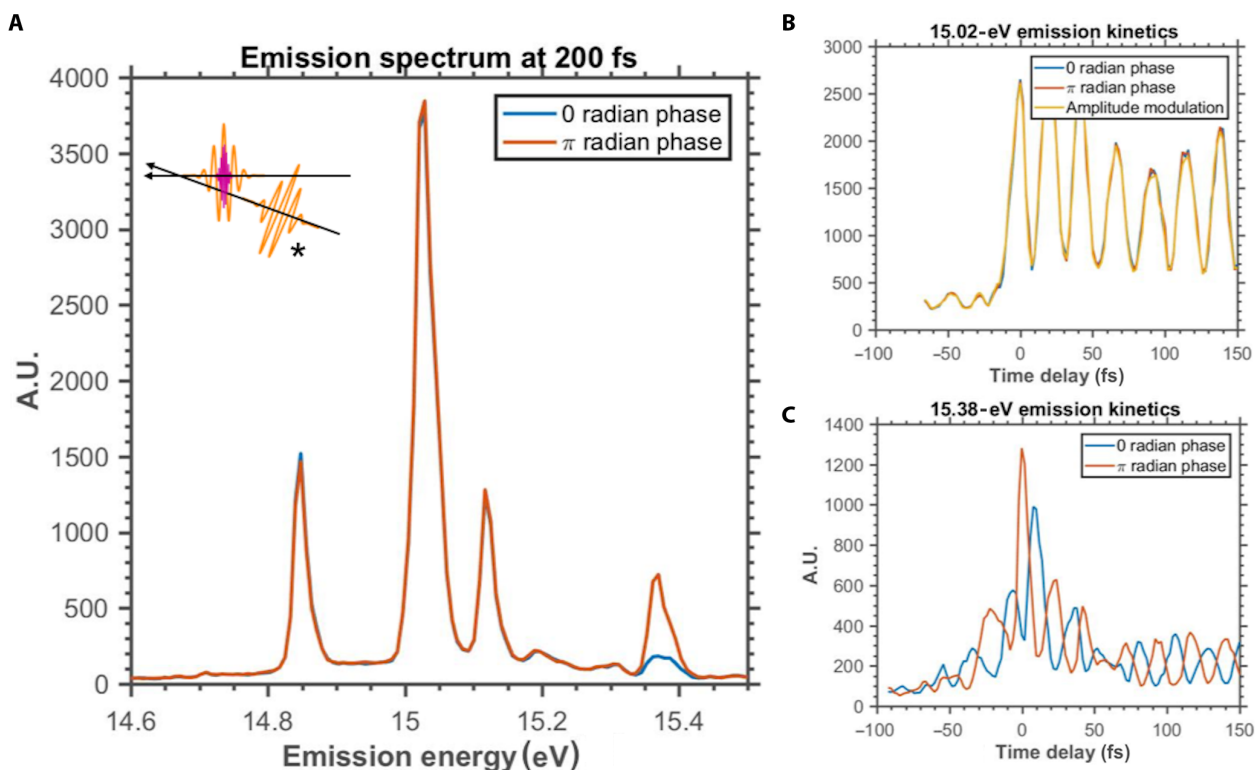
**Fig. 5. Effect of pulse shaping on time resolution.** (**A**) Dark-state 4WM signal spectrum at $T = 200$ fs with NIR pulse with 0 radian phase shaping (blue) and $\pi$ radian phase shaping. The beam geometry is shown in the inset. (**B**) Time evolution of the emission feature at 15.02 eV for the three types of modulations at 2.04 eV. The emission pathways at this energy are not resonant with the modulated NIR frequency; thus, the time traces are overlapped. (**C**) Time evolution of the emission feature at 15.38 eV for the two types of modulations at 2.04 eV. The pathways emitting at this energy are resonant with the shaped frequency and show strong modifications with phase shaping.

in the energy domain depends on the central frequency chosen in the NIR spectrum, since the diffraction gratings of the pulse shaper are linear in wavelength (*20*). The energy resolution on the XUV axis is determined by the 20-meV spectrometer resolution. The intensities of the peaks arise from the convolution of the XUV and NIR spectrum, of the different transition dipoles involved in the corresponding double-sided Feynman diagrams, and of the state dynamics at the time delay probed.

The time evolution of the feature at (14.85 eV; 1.76 eV) in the dark-state 2D spectrum taken using configuration I is shown in Fig. 4A, along with the time evolution of the total emission at 14.85 eV from the experiment without pulse shaping in Fig. 4B. The signal in Fig. 4B is the coherent sum of the emission pathways at 14.85 eV and therefore shows quantum beat oscillations of the interfering pathways. In the time evolution of the 2D feature, the quantum beats are eliminated. Derivation of the 2D signal in the Supplementary Materials shows that suppression in Fig. 4A of the quantum beats present in Fig. 4B implies that the signal probed by the 2D experiment originates from a single emission pathway and therefore probes the dynamics of a single state contained in the total wave packet. The Rydberg states considered are located below the first ionization potential of argon and therefore have population lifetimes and dephasing times in the gas phase that are orders of magnitude longer than the time delays investigated here. Consequently, the evolution of the states considered here appears constant. 2D spectra collected at various time delays are shown in fig. S3, which indicate that constant dynamics is observed across the different features of the 2D spectra.

To estimate the impact of pulse shaping on the time resolution of these experiments, we applied pulse shaping to a single group of 10 pixels centered at $\omega_{NIR} = 2.04$ eV for different time delays. The effect of a phase modulation at a time delay of 200 fs on the emission spectrum is shown in Fig. 5A. The phase modulation only affects the emission feature at 15.38 eV. This result is in agreement with the presence of a feature at (15.38 eV; 2.04 eV) in the 2D spectrum of Fig. 3B. The time evolution of the features at 15.02 and 15.38 eV is shown in Fig. 5 (B and C, respectively) for the various types of NIR pulses used in Eq. 1 to collect 2D spectra. The time evolution of the feature at 15.38 eV shows a phase shift of the oscillations with phase shaping. The feature at 15.02 eV shows no differences in time evolution for each of the shaped pulses, indicating that the 6-fs time resolution of the experiment is preserved.

We use configuration II to follow the time evolution of bright states created by the XUV pulse, as illustrated in the inset of Fig. 3C where $\tau$ and $T$ are each set to 60 fs. Because of the noncollinear beam geometry, the signal strength and signal-to-noise ratio in Fig. 3C are decreased compared to the partially collinear case in Fig. 3A, but the same emission lines are present in most regions. The 2D spectrum in Fig. 3D shows features at resonant NIR energies for all XUV emission frequencies. This horizontal line pattern reflects the idea that the second interaction in the double-sided Feynman diagram in Fig. 1E (that is, the lower orange arrow) is affected in this configuration. At a NIR frequency that is resonant between an initially prepared bright state and a $4p$ dark state, each pathway that includes this resonant frequency as its second interaction will result in a depletion in the 2D spectrum,

effectively creating the line pattern mentioned in Results. Because of the number of peaks arising at each resonant NIR frequency and the high density of states, the spectrum is congested and the interpretation is more complicated. Here, the peak intensities depend on the dynamics of the bright states as well as the spectra used and the transition dipole strengths; because of the lower signal-to-noise ratio in this configuration, no additional interpretation is given. Despite the congested spectrum, the expected line pattern is observed, showing that bright-state dynamics can also be probed.

Depending on the configuration used, the 2D experiments probe either a dark state (spectrum in Fig. 3B using configuration I) or a bright state (spectrum in Fig. 3D using configuration II). In Fig. 3B, the two features at (15.11 eV; 1.64 eV) and (14.85 eV; 1.76 eV) (blue circles) are attributed to the $[^2P_{3/2}]5d/7s \leftarrow [^2P_{1/2}]4p$ and $[^2P_{3/2}]4d \leftarrow [^2P_{3/2}]4p$ transitions, respectively. The NIR transitions are therefore associated with the dark state's time evolution, and the two features circled in Fig. 3B report on the dynamics of the $[^2P_{1/2}]4p$ and $[^2P_{3/2}]4p$ states, located at 13.47 and 13.09 eV, respectively. The time trace shown in Fig. 4B therefore reports on the dynamics of the $[^2P_{3/2}]4p$ state.

The shaped interaction in configuration II (Fig. 3D) probes the time evolution of the bright states; thus, the features in the 2D spectrum at 1.64 and 1.76 eV (blue arrows) probe the time evolution of $[^2P_{3/2}]5d/7s$ and $[^2P_{3/2}]4d$, located at 15.11 and 14.70 eV, respectively. In this configuration, a time delay ($\tau = 60$ fs) is introduced to reduce the time delay drift of the setup, as described in Results. During this time delay, the system is in the $4p$ dark states, which we show to have an invariant time evolution in Fig. 4A, and we expect no influence of this time delay on the probed dynamics.

In summary, using frequency-specific amplitude and phase modulations in one NIR interaction, the different pathways contributing to the 4WM signal emission are separated. The constructed 2D spectrum allows for retrieval of state-specific dynamics of bright or dark states, depending on the pulse ordering. The time evolution of the 2D spectral feature shows no quantum beat oscillations in this case of long-lived states, demonstrating an efficient separation of emission pathways. This technique follows the time evolution of individual states of the system in a regime where the optical field only acts as a probe, preventing field-induced effects such as state dressing and AC Stark effects and leaving the system's eigenstate dynamics as the only source of time evolution. It provides a tool for observing attosecond dynamics in a field-free regime where the only state couplings present are induced by nonadiabatic effects. Multidimensional information correlating absorption and emission allows for the potential observation of physics with direct analogy to other multidimensional experiments but here focused on pure electronic dynamics. In investigating systems with higher dimensionality where multiple states are excited by the XUV pulse, the time evolution of the 2D spectrum has the potential to reveal information about the energy redistribution among different excited states. While multidimensional experiments operating at optical frequencies are limited to investigating optically bright states, this experiment has the possibility of measuring lifetimes of short-lived optically dark states that are not easily observed.

## MATERIALS AND METHODS
The output of a titanium-sapphire laser (Femtopower, 1 kHz, 1.6 mJ, 20 fs, 790 nm) was broadened in a neon-filled hollow-core fiber to a spectrum spanning from 600 to 900 nm and compressed to a sub–6-fs

pulse duration by a set of double incidence angle chirp mirrors (UltraFast Innovations, PC70). Half of the 500-µJ beam was focused by a 500-mm-focal-length concave mirror into a xenon-filled gas cell to create a few-attosecond pulse train by amplitude-gated HHG. The remaining NIR radiation was removed by a 100-nm-thick indium filter (LeBow), and the transmitted XUV was focused onto the sample target by a gold-coated toroidal mirror. Considering an HHG conversion efficiency of $10^{-6}$ and after taking into account the optics in the apparatus, an output of 25 pJ was obtained, corresponding to $10^6$ photons per attosecond burst. At such a low number of photons per pulses, sequential excitation from consecutive attosecond pulses can be ruled out. The other half of the compressed beam was split by an uncoated wedged fused silica window. The reflected 4% was used as the unshaped beam, while the remaining 96% (240 µJ) was directed into the SLM-based pulse shaper (Meadowlark, D640-VN). The pulse shaper operates in a 4f geometry composed of two identical diffraction gratings (Richardson Gratings; 600 grooves/mm; blaze angle, 11.3°) and two $f = 200$-mm spherical concave mirrors. The beam intensity at the SLM was 150 µJ/cm$^2$, just under its damage threshold of 200 µJ/cm$^2$. The pulse shaper was aligned to minimize spatial chirp and divergence. The final grating position was tuned by optimizing second harmonic generation while maintaining good beam propagation. The original polarizers of the dual-mask 640-pixel SLM were removed and replaced by a broadband fused silica wire grid polarizer (Thorlabs, WP25M-UB) introduced in the beam path after the 4f geometry. The dispersion introduced by the SLM was corrected by the shaper itself by applying the opposite phase of the spectral phase determined by a commercial D-scan (Sphere) (21, 22). The shaped pulse conserves the input spectral bandwidth and was compressed to 5.5 fs with a total transmission of 15%. The pulse shaper was calibrated in two steps. One calibration of the voltage versus phase of each shaper's mask was done by recording the transmitted spectrum for the applied voltages (20). The wavelength versus pixel calibration was done day to day by recording the spectrum of the NIR pulse with a single pixel transmission set to unity (100% transmission) and the remaining pixels' transmission set to 0. This was repeated for all the pixels to retrieve the wavelength versus pixel relation across the SLM. To improve the beam focusing quality, a deformable mirror (Thorlabs, DMP40-P01) was used after the shaper to correct for astigmatism and higher-order aberrations (23). The shaped and unshaped NIR beams' time delays were controlled by two piezo-motorized delay stages (Physik Instrumente, P-622-1CL) and focused into the target cell by two spherical concave mirrors with a focal length of 1 m. The NIR beams were recombined with the XUV pulse by an annular mirror. Specifically, the XUV was transmitted through the mirror's aperture, while the two NIR beams were reflected above and below the hole. All three beams propagated in a common vertical plane. The two XUV-NIR angles were of approximately 1°. After the argon target gas cell, the NIR radiations were removed by a 100-nm-thick indium foil filter (LeBow). The XUV attosecond pulse and 4WM beams were dispersed by a cylindrical grating and imaged on an x-ray–grade CCD camera (Princeton Instruments, Pixis). The two XUV-NIR angles were large enough to separate the transmitted XUV pulse and 4WM emission signals on the camera so that no background subtraction was needed. For the 2D experiments, the spectra were obtained by collecting the 4WM XUV spectrum for the three types of pulses described in Results and by computing Eq. 1.

## SUPPLEMENTARY MATERIALS

Supplementary material for this article is available at http://advances.sciencemag.org/cgi/content/full/4/9/eaau3783/DC1

Fig. S1. Double-sided Feynman and Jablonski diagrams of two interfering pathways.
Fig. S2. Pulse characterization.
Fig. S3. Dark-state probing time evolution.

## REFERENCES AND NOTES

1. M. Uiberacker, T. Uphues, M. Schultze, A. J. Verhoef, V. Yakovlev, M. F. Kling, J. Rauschenberger, N. M. Kabachnik, H. Schröder, M. Lezius, K. L. Kompa, H. G. Muller, M. J. Vrakking, S. Hendel, U. Kleineberg, U. Heinzmann, M. Drescher, F. Krausz, Attosecond real-time observation of electron tunnelling in atoms. *Nature* **446**, 627–632 (2007).
2. A. Moulet, J. B. Bertrand, T. Klostermann, A. Guggenmos, N. Karpowicz, E. Goulielmakis, Soft x-ray excitonics. *Science* **357**, 1134–1138 (2017).
3. B. Bernhardt, A. R. Beck, X. Li, E. R. Warrick, M. J. Bell, D. J. Haxton, C. W. McCurdy, D. M. Neumark, S. R. Leone, High-spectral-resolution attosecond absorption spectroscopy of autoionization in xenon. *Phys. Rev. A* **89**, 023408 (2014).
4. C. Ott, A. Kaldun, P. Raith, K. Meyer, M. Laux, Y. Zhang, A. Blättermann, S. Hagstotz, T. Ding, R. Heck, J. Madroñero, F. Martín, T. Pfeifer, Reconstruction and control of a time-dependent two-electron wave packet. *Nature* **516**, 374–378 (2014).
5. M. Schultze, M. Fieß, N. Karpowicz, J. Gagnon, M. Korbman, M. Hofstetter, S. Neppl, A. L. Cavalieri, Y. Komninos, T. Mercouris, C. A. Nicolaides, R. Pazourek, S. Nagele, J. Feist, J. Burgdörfer, A. M. Azzeer, R. Ernstorfer, R. Kienberger, U. Kleineberg, E. Goulielmakis, F. Krausz, V. S. Yakovlev, Delay in photoemission. *Science* **328**, 1658–1662 (2010).
6. A. S. Johnson, D. R. Austin, D. A. Wood, C. Brahms, A. Gregory, K. B. Holzner, S. Jarosch, E. W. Larsen, S. Parker, C. S. Strüber, P. Ye, J. W. G. Tisch, J. P. Marangos, High-flux soft x-ray harmonic generation from ionization-shaped few-cycle laser pulses. *Sci. Adv.* **4**, eaar3761 (2018).
7. A. Sommer, E. M. Bothschafter, S. A. Sato, C. Jakubeit, T. Latka, O. Razskazovskaya, H. Fattahi, M. Jobst, W. Schweinberger, V. Shirvanyan, V. S. Yakovlev, R. Kienberger, K. Yabana, N. Karpowicz, M. Schultze, F. Krausz, Attosecond nonlinear polarization and light-matter energy transfer in solids. *Nature* **534**, 86–90 (2016).
8. E. R. Warrick, J. E. Bækhøj, W. Cao, A. P. Fidler, F. Jensen, L. Bojer Madsen, S. R. Leone, D. M. Neumark, Attosecond transient absorption spectroscopy of molecular nitrogen: Vibrational coherences in the $b'$ $^1\Sigma^+_u$ state. *Chem. Phys. Lett.* **683**, 408–415 (2017).
9. A. R. Beck, D. M. Neumark, S. R. Leone, Probing ultrafast dynamics with attosecond transient absorption. *Chem. Phys. Lett.* **624**, 119–130 (2015).
10. W. Cao, E. R. Warrick, A. Fidler, S. R. Leone, D. M. Neumark, Near-resonant four-wave mixing of attosecond extreme-ultraviolet pulses with near-infrared pulses in neon: Detection of electronic coherences. *Phys. Rev. A* **94**, 021802 (2016).
11. W. Cao, E. R. Warrick, A. Fidler, D. M. Neumark, S. R. Leone, Noncollinear wave mixing of attosecond XUV and few-cycle optical laser pulses in gas-phase atoms: Toward multidimensional spectroscopy involving XUV excitations. *Phys. Rev. A* **94**, 053846 (2016).
12. W. Cao, E. R. Warrick, A. Fidler, S. R. Leone, D. M. Neumark, Excited-state vibronic wave-packet dynamics in $H_2$ probed by XUV transient four-wave mixing. *Phys. Rev. A* **97**, 023401 (2018).
13. S. Bengtsson, E. W. Larsen, D. Kroon, S. Camp, M. Miranda, C. L. Arnold, A. L'Huillier, K. J. Schafer, M. B. Gaarde, L. Rippe, J. Mauritsson, Space–time control of free induction decay in the extreme ultraviolet. *Nat Photonics* **11**, 252–258 (2017).
14. M. Khalil, N. Demirdöven, A. Tokmakoff, Coherent 2D IR spectroscopy: Molecular structure and dynamics in solution. *J. Phys. Chem. A* **107**, 5258–5279 (2003).
15. R. M. Hochstrasser, Two-dimensional spectroscopy at infrared and optical frequencies. *Proc. Natl. Acad. Sci. U.S.A.* **104**, 14190–14196 (2007).
16. H. J. B. Marroux, B. F. E. Curchod, C. A. Faradji, T. A. Shuttleworth, H. A. Sparkes, P. G. Pringle, A. J. Orr-Ewing, Spin changes accompany ultrafast structural interconversion in the ground state of a cobalt nitrosyl complex. *Angew. Chem. Int. Engl.* **56**, 13713–13716 (2017).
17. G. S. M. Jansen, D. Rudolf, L. Freisem, K. S. E. Eikema, S. Witte, Spatially resolved Fourier transform spectroscopy in the extreme ultraviolet. *Optica* **3**, 1122–1125 (2016).
18. B. Schenkel, J. Biegert, U. Keller, C. Vozzi, M. Nisoli, G. Sansone, S. Stagira, S. De Silvestri, O. Svelto, Generation of 3.8-fs pulses from adaptive compression of a cascaded hollow fiber supercontinuum. *Opt. Lett.* **28**, 1987–1989 (2003).
19. F. Merkt, A. Osterwalder, R. Seiler, R. Signorell, H. Palm, H. Schmutz, R. Gunzinger, High Rydberg states of argon: Stark effect and field-ionization properties. *J. Phys. B At. Mol. Opt. Phys.* **31**, 1705 (1998).
20. A. M. Weiner, Ultrafast optical pulse shaping: A tutorial review. *Opt. Commun.* **284**, 3669–3692 (2011).
21. M. Miranda, C. L. Arnold, T. Fordell, F. Silva, B. Alonso, R. Weigand, A. L'Huillier, H. Crespo, Characterization of broadband few-cycle laser pulses with the d-scan technique. *Opt. Express* **20**, 18732–18743 (2012).
22. T. Binhammer, E. Rittweger, R. Ell, F. X. Kartner, U. Morgner, Prism-based pulse shaper for octave spanning spectra. *IEEE J. Quantum Electron.* **41**, 1552–1557 (2005).
23. M. J. Booth, Wavefront sensorless adaptive optics for large aberrations. *Opt. Lett.* **32**, 5–7 (2007).

**Citation:** H. J. B. Marroux, A. P. Fidler, D. M. Neumark, S. R. Leone, Multidimensional spectroscopy with attosecond extreme ultraviolet and shaped near-infrared pulses. *Sci. Adv.* **4**, eaau3783 (2018).